

Carbon Chain Chemistry in Hot-Core Regions around Three Massive Young Stellar Objects Associated with 6.7 GHz Methanol Masers

KOTOMI TANIGUCHI,¹ ERIC HERBST,^{2,3} LITON MAJUMDAR,⁴ PAOLA CASELLI,⁵ JONATHAN C. TAN,^{2,6} ZHI-YUN LI,² TOMOMI SHIMOIKURA,⁷ KAZUHITO DOBASHI,⁸ FUMITAKA NAKAMURA,^{9,10,11} AND MASAO SAITO^{9,10}

¹*Department of Physics, Faculty of Science, Gakushuin University, Mejiro, Toshima, Tokyo 171-8588, Japan*

²*Department of Astronomy, University of Virginia, Charlottesville, VA 22904, USA*

³*Department of Chemistry, University of Virginia, Charlottesville, VA 22903, USA*

⁴*School of Earth and Planetary Sciences, National Institute of Science Education and Research, HBNI, Jatni 752050, Odisha, India*

⁵*Max-Planck-Institute for Extraterrestrial Physics (MPE), Giessenbachstr, 1, D-85748 Garching, Germany*

⁶*Department of Space, Earth & Environment, Chalmers University of Technology, 412 93 Gothenburg, Sweden*

⁷*Faculty of Social Information Studies, Otsuma Women's University, Sanban-cho, Chiyoda, Tokyo 102-8357, Japan*

⁸*Department of Astronomy and Earth Sciences, Tokyo Gakugei University, Nukuikitamachi, Koganei, Tokyo 184-8501, Japan*

⁹*National Astronomical Observatory of Japan (NAOJ), National Institutes of Natural Sciences, Osawa, Mitaka, Tokyo 181-8588, Japan*

¹⁰*Department of Astronomical Science, School of Physical Science, SOKENDAI (The Graduate University for Advanced Studies), Osawa, Mitaka, Tokyo 181-8588, Japan*

¹¹*The University of Tokyo, Hongo, Bunkyo, Tokyo 113-0033, Japan*

(Received; Revised; Accepted)

Submitted to ApJ

ABSTRACT

We have carried out observations of CCH ($N = 1 - 0$), CH₃CN ($J = 5 - 4$), and three ¹³C isotopologues of HC₃N ($J = 10 - 9$) toward three massive young stellar objects (MYSOs), G12.89+0.49, G16.86-2.16, and G28.28-0.36, with the Nobeyama 45-m radio telescope. Combined with previous results on HC₅N, the column density ratios of $N(\text{CCH})/N(\text{HC}_5\text{N})$, hereafter the CCH/HC₅N ratios, in the MYSOs are derived to be ~ 15 . This value is lower than that in a low-mass warm carbon chain chemistry (WCCC) source by more than one order of magnitude. We compare the observed CCH/HC₅N ratios with hot-core model calculations (Taniguchi et al. 2019a). The observed ratios in the MYSOs can be best reproduced by models when the gas temperature is ~ 85 K, which is higher than in L1527, a low-mass WCCC source (~ 35 K). These results suggest that carbon-chain molecules detected around the MYSOs exist at least partially in higher temperature regions than those in low-mass WCCC sources. There is no significant difference in column density among the three ¹³C isotopologues of HC₃N in G12.89+0.49 and G16.86-2.16, while HCC¹³CN is more abundant than the others in G28.28-0.36. We discuss carbon-chain chemistry around the three MYSOs based on the CCH/HC₅N ratio and the ¹³C isotopic fractionation of HC₃N.

Keywords: astrochemistry – ISM: molecules – stars: massive

1. INTRODUCTION

Approximately 200 molecules have been identified in the interstellar medium and circumstellar shells (McGuire 2018). Around 40% of the interstellar molecules are accounted for by unsaturated carbon-chain molecules. Carbon-chain molecules, such as CCS and HC₅N, are generally known to be abundant in cold ($T \approx 10$ K) starless/prestellar cores (e.g., Suzuki et al. 1992; Benson et al. 1998). They are formed in the gas phase via ion-molecule reactions and exothermic neutral-neutral reactions without reaction energy barriers. Their abundances decrease in star-forming

cores (Suzuki et al. 1992; Benson et al. 1998), due to their destruction and/or depletion onto dust grains in cold high density regions just before protostars form. Based on the above characteristics, these carbon-chain species are also called “early-type species”.

Around protostars, partially saturated complex organic molecules (COMs), which consist of more than six atoms and are rich in hydrogen atoms, are abundant (Herbst & van Dishoeck 2009). These regions are referred to as hot cores and hot corinos in high-mass and low-mass star-forming regions, respectively. The COMs are formed on dust grains in the cold starless core and warm-up phases (Garrod & Herbst 2006; Garrod et al. 2008). Gas-phase reactions also contribute to the formation of COMs in both warm regions (e.g., Skouteris et al. 2019) and in cold environments (Balucani et al. 2015). Although general formation processes of COMs have been proposed, recent ALMA observations have revealed complexities of COM chemistry around protostars both in high-mass and low-mass star-forming regions (Jorgensen et al. 2020, and therein). For example, a chemical differentiation between N-bearing COMs and O-bearing COMs has been found (e.g., Crockett et al. 2015). Even among O-bearing COMs, there is a spatial segregation between COMs containing a C-O-C structure and those containing a C-OH bond (Tercero et al. 2018).

In contrast to hot corino chemistry, warm carbon chain chemistry (WCCC) was proposed initially around some low-mass protostars, such as L1527 and IRAS 15398–3359 (Sakai & Yamamoto 2013). In WCCC sources, carbon-chain molecules are efficiently formed from methane (CH_4) which is desorbed from dust grains at temperatures of $\sim 25 - 30$ K (Hassel et al. 2008). Reactions between CH_4 molecules and C^+ ions initiate carbon-chain formation in the lukewarm gas ($T \approx 25 - 30$ K). In high-mass star-forming regions, observational studies concerning carbon-chain chemistry are less well developed. It is unknown whether carbon-chain molecules are formed anew around massive young stellar objects (MYSOs), and if they are formed, whether these carbon-chain molecules exist in higher temperature regions than those in low-mass WCCC sources.

Green et al. (2014) carried out survey observations of HC_5N toward MYSOs containing 6.7 GHz CH_3OH masers. They detected HC_5N in 35 sources out of 79 MYSOs using the $J = 12 - 11$ line (31.951777 GHz; $E_{\text{up}}/k = 9.97$ K) with the 34-m radio telescope at Tidbinbilla. However, the detected HC_5N lines seem to come mainly from cold envelopes ($T \approx 10$ K), not from inner hot regions, because of the large beam size ($0.95'$) and the low energy level of the observed line. Taniguchi et al. (2018c) detected HC_5N in 14 high-mass protostellar objects (HMPOs) out of 35 sources using the $J = 16 - 15$ line (42.60215 GHz; $E_{\text{up}}/k = 17.4$ K) with the Nobeyama 45-m telescope and a beam size of $37''$. However, this line also may come from cold envelopes, and it was unclear whether HC_5N is in warm ($T \approx 25$ K) and/or hot ($T \gtrsim 100$ K) regions.

Taniguchi et al. (2017b) also carried out observations of HC_5N toward four MYSOs with the Green Bank 100-m and the Nobeyama 45-m radio telescopes. They detected several lines with high upper state energies that are difficult to be excited in cold regions (e.g., $J = 39 - 38$; $E_{\text{up}}/k = 99.7$ K). These results suggest that HC_5N exists in warm and/or hot regions around MYSOs. However, their observations were conducted with single-dish telescopes and it could not be strongly concluded that the detected HC_5N around MYSOs exists in higher temperature regions than found in low-mass WCCC sources. Taniguchi et al. (2018a) investigated the spatial distributions of HC_3N and HC_5N in the G28.28–0.36 MYSO, and their spatial distributions are positively correlated with the dust continuum emission. These results support the possibility of gas-phase cyanopolyne formation (HC_{2n+1}N , $n = 1, 2, 3, \dots$) in warm regions from dust-origin precursors.

Recently, Taniguchi et al. (2019a) conducted gas-grain chemical network simulations in order to investigate the carbon-chain chemistry around MYSOs in detail. Based on these time-dependent calculations, they suggested that there are largely two types of carbon-chain species. During the warm-up period, cyanopolyynes, which are relatively stable species, are formed in the gas phase, depleted onto dust grains and condensed in ice mantles during the lukewarm phase ($25 \text{ K} < T < 100 \text{ K}$). After their sublimation temperature is reached ($T \geq 100 \text{ K}$), cyanopolyynes are desorbed from dust grains and their gas-phase abundances show peak values. On the other hand, CCH is efficiently formed and shows its peak abundance in a WCCC-like region just after the temperature reaches 25 K, at which temperature the CH_4 molecules are desorbed from dust grains. The CCH radicals are rapidly formed by the electron recombination reaction of C_2H_3^+ , which is formed by the reaction between CH_4 and C^+ . After the temperature exceeds 70 K, CCH is efficiently destroyed by atomic oxygen (O). The main destroyer of CCH becomes H_2 at temperatures above 90 K, and destruction becomes much faster. Motivated by this model calculation (Taniguchi et al. 2019a), we infer that the CCH/ HC_5N ratio can be used as a temperature probe over the range where these carbon-chain molecules exist. This ratio is expected to decrease with an increase in temperature. Hence, if HC_5N around MYSOs exists to a greater extent

Table 1. Summary of target sources

Source	R.A. (J2000)	Decl. (J2000)	D (kpc)	V_{sys}^d (km s^{-1})	L (L_{\odot})	M_{clump} (M_{\odot})	Spectral Type
G12.89+0.49	18 ^h 11 ^m 51 ^s .4	-17°31'30"	2.94 ^a	33.3	$3.3 \times 10^4{}^e$	1505 ^e	B0 ^g
G16.86-2.16	18 ^h 29 ^m 24 ^s .4	-15°16'04"	1.7 ^b	17.8	$3.2 \times 10^3{}^f$	437 ^b	B2 ^g
G28.28-0.36	18 ^h 44 ^m 13 ^s .3	-04°18'03"	3.0 ^c	48.9	... ^h	723 ⁺¹²⁴ ₋₁₁₆ ^h	...

^aTaken from [Immer et al. \(2013\)](#).

^bTaken from [Urquhart et al. \(2015\)](#).

^cTaken from [Green et al. \(2014\)](#).

^dTaken from [Purcell et al. \(2006\)](#).

^eThe mass and luminosity at the distance of 3.3 kpc are taken from [Lu et al. \(2014\)](#). We converted these values into those at a distance of 2.94 kpc. The luminosity is indicated as L_{IR} in [Lu et al. \(2014\)](#).

^fThe luminosity of G16.86-2.16 at a distance of 1.9 kpc is taken from [Purcell et al. \(2006\)](#). We converted it into the value at a distance of 1.7 kpc.

^gThe approximate spectral types for a given luminosity are given in Table 1 in [Panagia \(1973\)](#).

^hThe mass at a distance of 3.29 kpc is taken from [Cyganowski et al. \(2011\)](#). We converted it into that at a distance of 3.0 kpc. The bolometric luminosity could not be derived, because a clear counterpart is not present or because confusion/blending precludes measuring a reliable flux for the EGO counterpart. The dust temperature was assumed to be 28 K.

in higher temperature regions than in lukewarm regions around low-mass WCCC sources, the CCH/HC₅N ratios in MYSOs will be lower than those in WCCC sources.

In this paper, we report new observations of CCH ($N = 1 - 0$), CH₃CN ($J = 5 - 4$), and three ¹³C isotopologues of HC₃N ($J = 10 - 9$) toward three MYSOs (G12.89+0.49, G16.86-2.16, and G28.28-0.36) with the Nobeyama 45-m radio telescope. We describe the observations in Section 2. The spectra of the above three species are presented in Section 3.1, and analytical methods and results are summarized in Section 3.2. In combination with previous results on HC₅N reported by [Taniguchi et al. \(2017b\)](#), we derive the CCH/HC₅N ratios toward the three MYSOs. These CCH/HC₅N ratios toward the three MYSOs are compared with those in a low-mass WCCC source L1527 in Section 4.1, and with the model calculation in Section 4.2. In Section 4.3, the differences in column density among the three ¹³C isotopologues of HC₃N, namely the ¹³C isotopic fractionation, and possible main formation pathways of HC₃N are presented. We discuss carbon-chain chemistry around the three MYSOs based on the CCH/HC₅N ratio and the ¹³C isotopic fractionation of HC₃N in Section 4.4. The main conclusions of this paper are summarized in Section 5.

2. OBSERVATIONS

The observations presented in this paper were carried out with the Nobeyama 45-m radio telescope in 2019 April and May (2018-2019 semester¹). Our three target MYSOs are the sources observed by [Taniguchi et al. \(2017b, 2018b\)](#). The properties of the target sources are summarized in Table 1. These sources were selected with the following criteria:

1. The source declination is above -21° ,
2. the distance (D) is within 3 kpc, and
3. CH₃CN was detected with the Mopra telescope ($\int T_{\text{mb}} dv > 0.5 \text{ K km s}^{-1}$ for the $J_K = 5_0 - 4_0$ line; [Purcell et al. 2006](#)).

¹ Proposal ID; SP189002, PI; Kotomi Taniguchi

In addition, the 6.7 GHz CH₃OH maser and molecular outflows are associated with all of the sources (Cyganowski et al. 2008; Li et al. 2016). The 6.7 GHz CH₃OH maser is known as a sign of massive star formation (Urquhart et al. 2015). The G28.28–0.36 MYSO is categorized as a GLIMPSE Extended Green Object (EGO; Cyganowski et al. 2011).

We used the FOREST receiver (Minamidani et al. 2016) in the on-on observing mode². The integration time for each scan was 20 seconds. The off-source positions for calibrating observations were set at +15′ away in declination. The main beam efficiency (η_{mb}) and the beam size (HPBW) at 86 GHz of this receiver are $\sim 50\%$ and 18″, respectively. The system temperatures were between ~ 200 K and ~ 250 K, depending on weather conditions and elevation.

We used the SAM45 FX-type digital correlator in a frequency setup, the bandwidth and frequency resolution of which are 500 MHz and 122.07 kHz, respectively. This frequency resolution corresponds to a velocity resolution of 0.4 km s^{-1} at the observed frequency range. We conducted 2-channel binning in the final spectra, and the velocity resolution of the final spectra is $\sim 0.8 \text{ km s}^{-1}$.

The telescope pointing was checked every 1.5 hr by observing the SiO maser line ($J = 1 - 0$; 43.12203 GHz) from OH39.7+1.5 at $(\alpha_{2000}, \delta_{2000}) = (18^{\text{h}}56^{\text{m}}03^{\text{s}}.88, +06^{\circ}38'49''.8)$. The H40 receiver was used for the pointing observations. The pointing errors were within 3″.

3. RESULTS AND ANALYSES

3.1. Results

We analyzed spectra with the Java NEWSTAR, which is a software package for data reduction and analyses of the Nobeyama 45-m radio telescope³. The total integration times are approximately 9 hours, 6 hours, and 7 hours, for G12.89+0.49, G16.86–2.16, and G28.28–0.36, respectively.

Figures 1–3 show spectra of CCH ($N = 1 - 0$), three ¹³C isotopologues of HC₃N ($J = 10 - 9$), and CH₃CN ($J = 5 - 4$), respectively, toward the three MYSOs. The rms noise levels are 4–5 mK in T_{A}^* scale in all of the sources. We fitted the spectra with a Gaussian profile. The obtained spectral line parameters are summarized in Table 2. We applied a main beam efficiency (η_{mb}) of 50%, 46%, and 48% to the CCH, CH₃CN, and three ¹³C isotopologues of HC₃N lines, respectively, for calculation of T_{mb} values. These η_{mb} values were calculated by extrapolation using the reported values at 86 GHz and 110 GHz⁴.

The observed radial velocities (V_{LSR}) of each line are consistent with the systemic velocities of each source (Table 1) within the errors. The $J_K = 5_3 - 4_3$ line of CH₃CN in G28.28–0.36 shows a slightly larger V_{LSR} value compared with the systemic velocity, but this is due to the low signal-to-noise (S/N) ratio of this line.

Six lines of the hyperfine and fine structures of CCH have been detected from the three MYSOs as shown in Figure 1. Their line widths (Δv) obtained by the Gaussian fitting are $\sim 3 - 3.5 \text{ km s}^{-1}$ in G12.89+0.49 and G16.86–2.16, and $\sim 2.5 - 3 \text{ km s}^{-1}$ in G28.28–0.36, respectively (see Table 2). These values agree with line widths of other carbon-chain molecules (Taniguchi et al. 2017b, 2018b). In addition, these line widths are consistent with typical line widths of molecular lines in hot cores.

All of the three ¹³C isotopologues of HC₃N have been detected with S/N ratios above 10 in G12.89+0.49 and G16.86–2.16, and S/N ratios between 6 and 9 in G28.28–0.36 (Figure 2). Their line widths are consistent with the main isotopologue of the same transition ($J = 10 - 9$; Taniguchi et al. 2018b) within the errors.

Five K -ladder lines ($K = 0 - 4$) of CH₃CN have been detected from G12.89+0.49 and G16.86–2.16, and four lines, missing the $J_K = 5_4 - 4_4$ line, were detected from G28.28–0.36, as shown in the upper panels of Figure 3. The line widths of the $K = 0$ line are in good agreement with those of carbon-chain species (CCH, HC₃N, and HC₅N), while the higher K -value lines show wider spectral features. These results suggest that the lines with higher upper energy levels come from inner hot regions.

3.2. Analyses

We describe analytical methods and present results in this subsection. The derived column densities and excitation temperatures are summarized in Table 3. These derived column densities are the averaged values with a beam size of 18″, in the same manner as previous studies (Taniguchi et al. 2017b, 2018b).

3.2.1. CCH

² <https://www.nro.nao.ac.jp/~nro45mrt/html/obs/nobs/scan.html#on-on>

³ <https://www.nro.nao.ac.jp/~jnewstar/html/>

⁴ <https://www.nro.nao.ac.jp/~nro45mrt/html/prop/eff/eff2019.html>

Table 2. Spectral line parameters

Species	Frequency ^a	E_{up}/k	G12.89+0.49				G16.86–2.16				G28.28–0.36			
			T_{mb}	Δv^b	$\int T_{\text{mb}} dv$	V_{LSR}	T_{mb}	Δv^b	$\int T_{\text{mb}} dv$	V_{LSR}	T_{mb}	Δv^b	$\int T_{\text{mb}} dv$	V_{LSR}
Transition	(GHz)	(K)	(K)	(km s ⁻¹)	(K km s ⁻¹)	(km s ⁻¹)	(K)	(km s ⁻¹)	(K km s ⁻¹)	(km s ⁻¹)	(K)	(km s ⁻¹)	(K km s ⁻¹)	(km s ⁻¹)
CCH														
$J = \frac{3}{2} - \frac{1}{2}$,														
$F = 1 - 1$	87.284156	4.2	0.341 (15)	3.06 (16)	1.15 (14)	33.7 (1)	0.36 (3)	3.1 (3)	1.2 (2)	17.3 (1)	0.359 (17)	2.12 (12)	0.86 (11)	49.4 (1)
$F = 2 - 1$	87.316925	4.2	1.548 (13)	3.66 (4)	6.2 (6)	33.1 (1)	2.69 (3)	2.73 (4)	8.1 (8)	17.5 (1)	1.272 (15)	2.91 (4)	4.1 (4)	49.6 (1)
$F = 1 - 0$	87.328624	4.2	1.042 (14)	3.39 (5)	3.9 (4)	33.0 (1)	1.30 (3)	3.38 (10)	4.8 (5)	17.4 (1)	0.852 (16)	2.53 (6)	2.4 (2)	49.6 (1)
$J = \frac{1}{2} - \frac{1}{2}$,														
$F = 1 - 1$	87.402004	4.2	1.035 (14)	3.36 (5)	3.8 (4)	33.5 (1)	1.28 (3)	3.32 (10)	4.7 (5)	17.1 (1)	0.893 (16)	2.52 (5)	2.5 (3)	49.2 (1)
$F = 0 - 1$	87.407165	4.2	0.556 (15)	3.04 (9)	1.9 (2)	32.8 (1)	0.65 (3)	3.07 (19)	2.2 (3)	17.2 (1)	0.551 (17)	2.15 (8)	1.35 (15)	49.3 (1)
$F = 1 - 0$	87.446512	4.2	0.336 (15)	2.99 (16)	1.11 (13)	33.8 (1)	0.35 (3)	3.1 (3)	1.2 (2)	17.3 (1)	0.335 (17)	2.20 (14)	0.83 (11)	49.5 (1)
H ¹³ CCCN														
$J = 10 - 9$	88.166832	23.3	0.103 (6)	3.7(3)	0.41 (6)	32.4 (1)	0.092 (7)	3.1 (3)	0.31 (5)	17.3 (1)	0.052 (9)	2.4 (5)	0.14 (4)	49.1 (1)
HC ¹³ CCN														
$J = 10 - 9$	90.593059	23.9	0.111 (5)	3.9 (2)	0.46 (6)	33.3 (1)	0.100 (6)	3.0 (2)	0.33 (5)	17.0 (1)	0.076 (9)	1.6 (2)	0.15 (3)	49.0 (1)
HCC ¹³ CN														
$J = 10 - 9$	90.601777	23.9	0.103 (5)	3.7 (2)	0.42 (5)	32.3 (1)	0.096 (6)	3.2 (3)	0.33 (5)	17.5 (1)	0.071 (8)	2.3 (3)	0.18 (4)	49.5 (1)
CH ₃ CN														
$J_K = 5_4 - 4_4$	91.9587260	127.5	0.116 (6)	8.2 (5)	1.01 (13)	31.0 (1)	0.050 (8)	9.5 (1.8)	0.51 (14)	17.3 (2)
$J_K = 5_3 - 4_3$	91.9711304	77.5	0.353 (7)	6.23 (14)	2.4 (2)	34.1 (1)	0.188 (10)	6.5 (4)	1.3 (2)	17.9 (1)	0.030 (6)	4.5 (1.0)	0.14 (5)	50.3 (4)
$J_K = 5_2 - 4_2$	91.9799943	41.8	0.410 (7)	5.52 (11)	2.4 (3)	32.7 (1)	0.254 (11)	5.3 (3)	1.5 (2)	17.4 (1)	0.075 (7)	2.8 (3)	0.23 (4)	49.0 (2)
$J_K = 5_1 - 4_1$	91.9853141	20.4	0.614 (7)	5.88 (9)	3.9 (4)	32.5 (2)	0.493 (12)	4.83 (15)	2.6 (3)	17.2 (2)	0.219 (8)	2.35 (10)	0.58 (7)	49.6 (3)
$J_K = 5_0 - 4_0$	91.9870876	13.2	0.651 (9)	3.68 (6)	2.6 (3)	32.8 (2)	0.587 (13)	3.73 (11)	2.4 (3)	17.4 (2)	0.264 (8)	2.10 (8)	0.63 (7)	49.0 (3)

NOTE—Numbers in parentheses are the standard deviation, expressed in units of the last significant digits. The standard deviation for T_{mb} and Δv is derived from the Gaussian fit, and we derived the standard deviation for $\int T_{\text{mb}} dv$ taking the standard deviation of T_{mb} and Δv and 10% absolute calibration errors due to the chopper-wheel calibration into consideration.

^a Rest frequency and excitation energy are taken from the Cologne Database for Molecular Spectroscopy (CDMS; Müller et al. 2005) for the lines of CCH and ¹³C isotopologues of HC₃N, and the Jet Propulsion Laboratory (JPL) catalog (Pickett et al. 1998) for the CH₃CN lines.

^b Line widths are calculated using the following formula: $\Delta v = \sqrt{\Delta v_{\text{gau}}^2 - \Delta v_{\text{inst}}^2}$, where Δv_{gau} and Δv_{inst} are the line widths obtained by the Gaussian fit and the instrumental velocity resolution (0.8 km s⁻¹), respectively.

CARBON CHAIN CHEMISTRY IN HOT CORE REGIONS AROUND MYOS

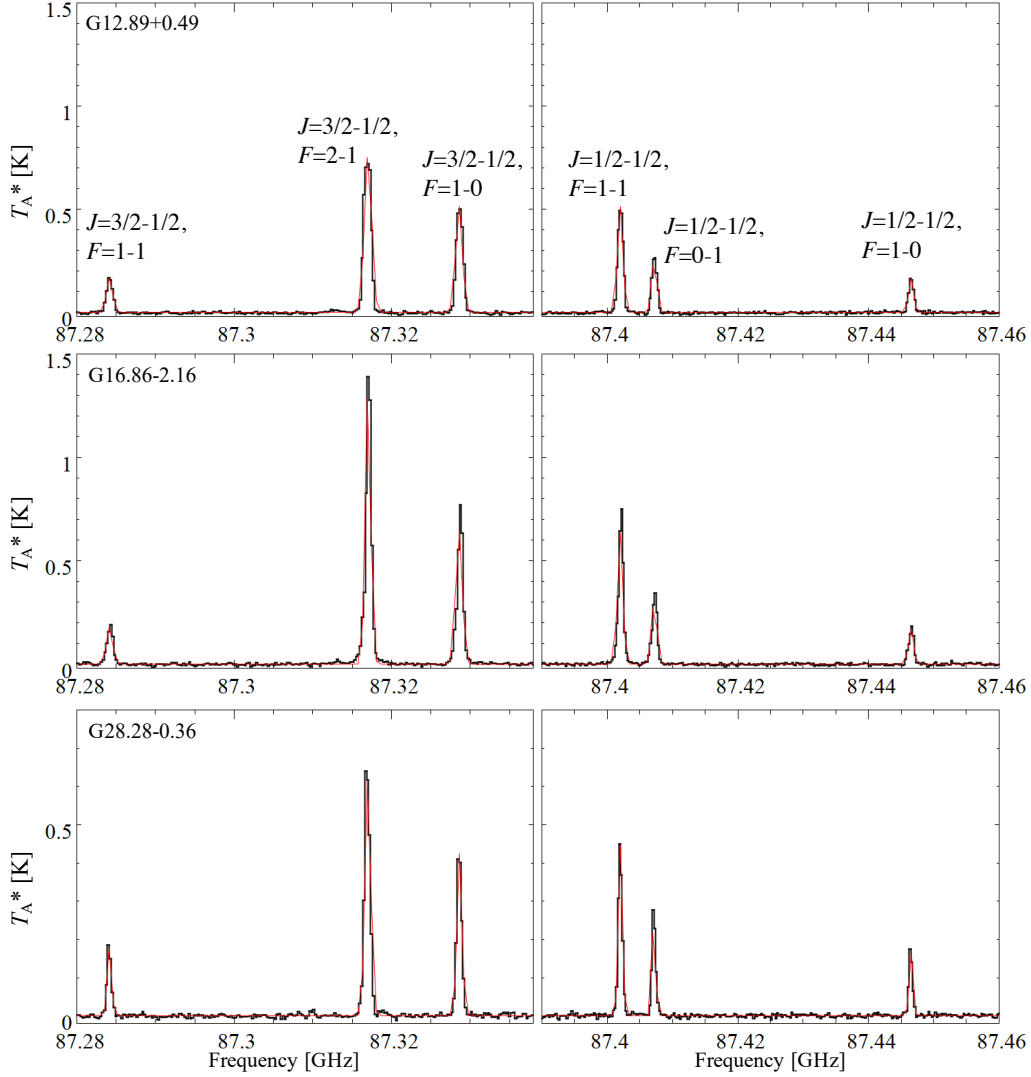


Figure 1. Spectra of the CCH ($N = 1 - 0$) lines toward the three MYSOs obtained with the Nobeyama 45-m radio telescope. The red curves indicate the results of the Gaussian fit. $J = N \pm \frac{1}{2}$ (except for $N = 0$, when $J = \frac{1}{2}$ only), and $F = J \pm \frac{1}{2}$. J couples electronic spin with rigid rotation, while F couples nuclear spin.

We derived excitation temperatures and column densities of CCH using the RADEX code (van der Tak et al. 2007). We assumed that the gas kinetic temperatures (T_{gas}) are equal to the excitation temperatures of CH_3CCH , $T_{\text{ex}}(\text{CH}_3\text{CCH})$, derived by the rotational diagram method using the K -ladder lines of the $J = 5 - 4$ and $6 - 5$ transitions (Taniguchi et al. 2018b). The $T_{\text{ex}}(\text{CH}_3\text{CCH})$ values were derived to be 33_{-9}^{+20} K, 29_{-8}^{+15} K, and 23_{-6}^{+9} K in G12.89+0.49, G16.86–2.16, and G28.28–0.36, respectively. The line widths of CCH are comparable to those of CH_3CCH , which supports the hypothesis that these species trace similar temperature regions and our assumption that T_{gas} can be set at $T_{\text{ex}}(\text{CH}_3\text{CCH})$.

The chemical model calculations (Taniguchi et al. 2019a) indicate that carbon-chain species are formed in the lukewarm ($T > 25$ K) region, where the CH_4 molecules are desorbed from dust grains, as in WCCC regions. In such temperature ranges, the lowest H_2 density was estimated to be $\sim 10^5 \text{ cm}^{-3}$ based on hot-core models by Nomura & Millar (2004). We then assumed that the H_2 density is $1 \times 10^5 \text{ cm}^{-3}$ at first.

With the above conditions ($n(\text{H}_2) = 1 \times 10^5 \text{ cm}^{-3}$ and $T_{\text{gas}} = 33$ K, 29 K, and 23 K in G12.89+0.49, G16.86–2.16, and G28.28–0.36, respectively), the derived excitation temperatures of CCH in G12.89+0.49 and G16.86–2.16 are higher than the assumed T_{gas} values (case a in Table 3). In G28.28–0.36, the column density and excitation temperature of CCH are $(2.8 \pm 1.1) \times 10^{14} \text{ cm}^{-2}$ and 16 ± 3 K.

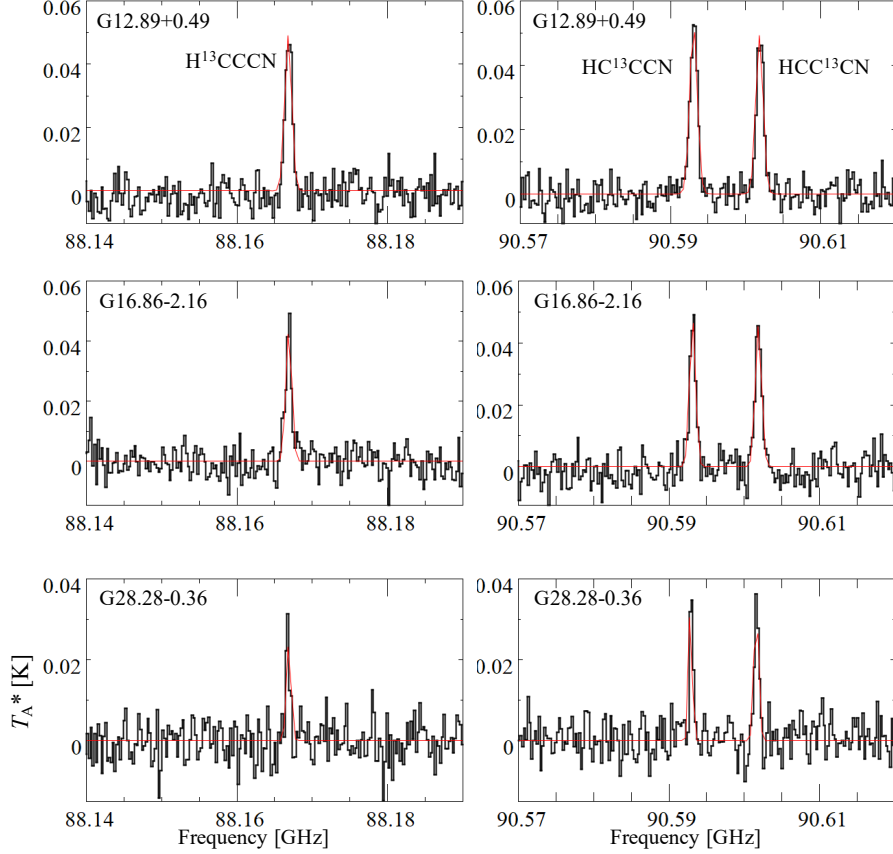


Figure 2. Spectra of three ^{13}C isotopologues of HC_3N ($J = 10 - 9$) toward the three MYSOs obtained with the Nobeyama 45-m radio telescope. The red curves indicate the results of the Gaussian fit.

Next, we reduced the H_2 density to $5 \times 10^4 \text{ cm}^{-3}$ and derived the column densities and excitation temperatures of CCH (case b in Table 3). The column densities and excitation temperatures of CCH are derived to be $(4.1 \pm 1.4) \times 10^{14} \text{ cm}^{-2}$ and $13 \pm 2 \text{ K}$ in G12.89+0.49, and $(5.1 \pm 1.0) \times 10^{14} \text{ cm}^{-2}$ and $11 \pm 2 \text{ K}$ in G16.86-2.16, respectively. The column density of CCH is derived to be $(3.1 \pm 1.3) \times 10^{14} \text{ cm}^{-2}$ in G28.28-0.36. The column densities of CCH do not change and are in agreement for cases a and b within their errors.

Finally, we tried T_{gas} values at the lower limits of $T_{\text{ex}}(\text{CH}_3\text{CCH})$ - 24 K in G12.89+0.49, 21 K in G16.86-2.16, and 17 K in G28.28-0.36 - and an H_2 density of $1 \times 10^5 \text{ cm}^{-3}$ (case c in Table 3). The derived column densities of CCH do not change significantly among all of the sets of assumed physical parameters. The results are consistent within their errors in all of the sources.

In the density range between $5 \times 10^4 \text{ cm}^{-3}$ and 10^6 cm^{-3} , the derived column densities of CCH increase by only a factor of two at $n(\text{H}_2) = 10^6 \text{ cm}^{-3}$. Thus, the assumed physical parameters do not change the column densities of CCH significantly, and our following discussions are not affected.

3.2.2. ^{13}C isotopologues of HC_3N

Taniguchi et al. (2018b) derived the column densities and rotational temperatures of the main isotopologue of HC_3N , including the $J = 10 - 9$ line, toward the same MYSOs using the rotational diagram method under LTE conditions by following Goldsmith & Langer (1999). Here, we assume that the spatial distributions of the ^{13}C isotopologues are the same as the main isotopologue and apply the LTE assumption for simplicity. We used the following formulae (Taniguchi et al. 2016a):

$$\tau = -\ln \left[1 - \frac{T_{\text{mb}}}{J(T_{\text{ex}}) - J(T_{\text{bg}})} \right] \quad (1)$$

where

$$J(T) = \frac{h\nu}{k} \left\{ \exp\left(\frac{h\nu}{kT}\right) - 1 \right\}^{-1}, \quad (2)$$

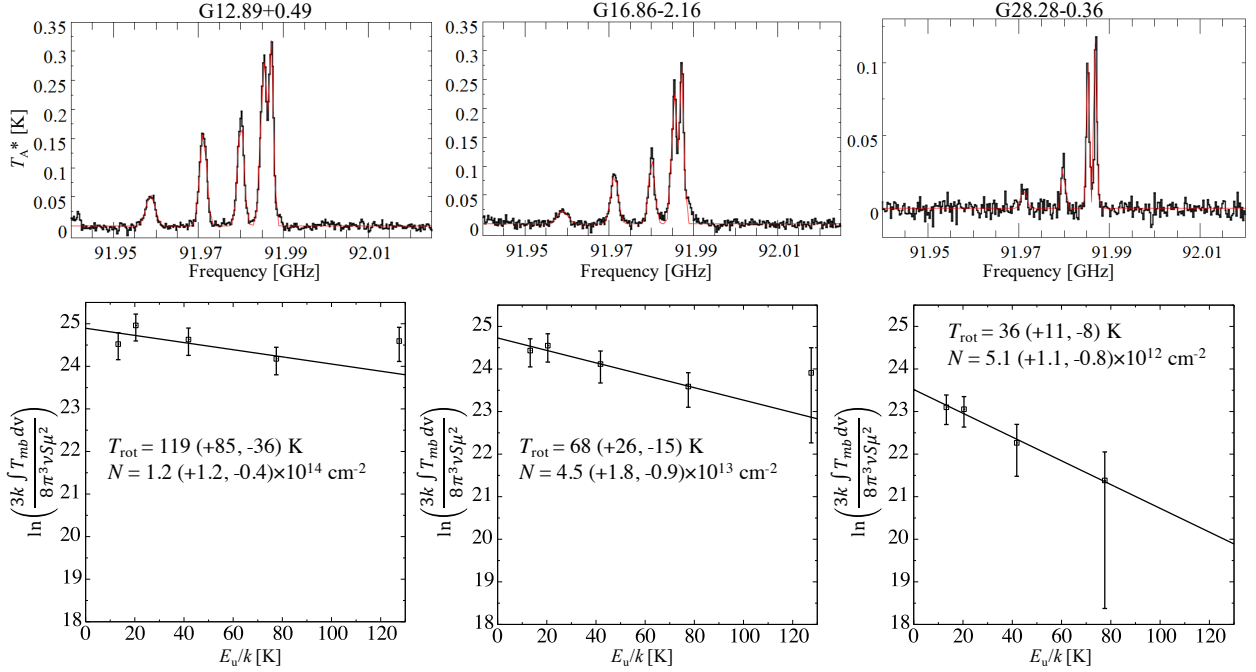


Figure 3. The top panels show spectra of CH_3CN ($J = 5 - 4$, K -ladder lines) toward the three MYSOs obtained with the Nobeyama 45-m radio telescope. The red curves show the results of the Gaussian fitting of spectra. The bottom panels show the rotational diagram for each source. The error bars for each data point represent 3σ errors.

and

$$N = \tau \frac{3h\Delta v}{8\pi^3} \sqrt{\frac{\pi}{4\ln 2}} Q \frac{1}{\mu^2} \frac{1}{J_{\text{lower}} + 1} \exp\left(\frac{E_{\text{lower}}}{kT_{\text{ex}}}\right) \left\{ 1 - \exp\left(-\frac{h\nu}{kT_{\text{ex}}}\right) \right\}^{-1}. \quad (3)$$

In Equation (1), τ denotes the optical depth, and T_{mb} represents the peak intensities summarized in Table 2. The excitation temperature and the cosmic microwave background temperature ($\simeq 2.73$ K) are indicated as T_{ex} and T_{bg} , respectively. We assumed that the excitation temperatures of the ^{13}C isotopologues of HC_3N are equal to the rotational temperatures of the main isotopologue (Taniguchi et al. 2018b); 24 K, 20 K, and 13.4 K in G12.89+0.49, G16.86–2.16, and G28.28–0.36, respectively. Since we have considered the latest result on T_{ex} for HC_3N (Taniguchi et al. 2018b) as the most plausible, we used their results here. $J(T)$ in Equation (2) is the effective temperature equivalent to that in the Rayleigh-Jeans law. The symbols of h , k , and ν denote the Planck constant, Boltzmann constant, and rest frequency, respectively. In Equation (3), N is the column density, Δv is the line width (Table 2), Q is the rotational partition function, μ is the permanent electric dipole moment, and E_{lower} is the energy of the lower rotational energy level. We assume that the electric dipole moments of the ^{13}C isotopologues of HC_3N are equal to that of the main isotopologue (3.73172 D; DeLeon & Muentner 1985).

The derived column densities are summarized in Table 3. In G12.89+0.49 and G16.86–2.16, the column densities of the three ^{13}C isotopologues are consistent with each other in each source. On the other hand, HCC^{13}CN is slightly more abundant than the others in G28.28–0.36, which agrees with the previous results (Taniguchi et al. 2016b).

In these observations, we observed only one rotational line for each ^{13}C isotopomer, and derived the column densities by fixing the excitation temperatures. Hence, the absolute values of column densities may contain extra uncertainties due to the assumed T_{ex} value. However, these uncertainties do not affect our discussion, because we focus on the ^{13}C isotopic fractionation of HC_3N , or relative differences in abundance among the ^{13}C isotopologues, which are expected to trace the same conditions. Relative abundances are not affected by the assumed excitation temperature or absolute column densities, when we compare them using the same transition.

The derived column densities in G28.28–0.36 reported here and those of Taniguchi et al. (2016b) differ. This is caused by the different assumed excitation temperatures. We believe that the column densities derived here are more reliable, because Taniguchi et al. (2016b) assumed that the excitation temperature is 100 K, a typical hot core temperature. As mentioned before, the different values of column density do not affect our discussion. Our final conclusion using ^{13}C isotopic fractionation (Section 4.3) is consistent with that of Taniguchi et al. (2016b).

Table 3. Column density and excitation temperature in three MYSOs

Species	G12.89+0.49		G16.86–2.16		G28.28–0.36	
	N (cm $^{-2}$)	T_{ex} (K)	N (cm $^{-2}$)	T_{ex} (K)	N (cm $^{-2}$)	T_{ex} (K)
CCH ^a	$(4.2 \pm 1.4) \times 10^{14}$	40 ± 15	$(4.9 \pm 1.1) \times 10^{14}$	26 ± 6	$(2.8 \pm 1.1) \times 10^{14}$	16 ± 3
CCH ^b	$(4.1 \pm 1.4) \times 10^{14}$	13 ± 2	$(5.1 \pm 1.0) \times 10^{14}$	11 ± 2	$(3.1 \pm 1.3) \times 10^{14}$	9 ± 1
CCH ^c	$(3.9 \pm 1.3) \times 10^{14}$	17 ± 3	$(4.8 \pm 0.9) \times 10^{14}$	14 ± 2	$(2.9 \pm 1.2) \times 10^{14}$	11 ± 1
H ¹³ CCCN	$(1.8 \pm 0.2) \times 10^{12}$	24^d	$(1.4 \pm 0.2) \times 10^{12}$	20^d	$(7.6 \pm 2.1) \times 10^{11}$	13.4^d
HC ¹³ CCN	$(1.9 \pm 0.2) \times 10^{12}$	24^d	$(1.4 \pm 0.2) \times 10^{12}$	20^d	$(7.9 \pm 1.6) \times 10^{11}$	13.4^d
HCC ¹³ CN	$(1.8 \pm 0.2) \times 10^{12}$	24^d	$(1.4 \pm 0.2) \times 10^{12}$	20^d	$(9.97 \pm 1.9) \times 10^{11}$	13.4^d
CH ₃ CN	$1.2_{-0.4}^{+1.2} \times 10^{14}$	119_{-36}^{+85}	$4.5_{-0.9}^{+1.8} \times 10^{13}$	68_{-15}^{+26}	$5.1_{-0.8}^{+1.1} \times 10^{12}$	36_{-8}^{+11}

NOTE—The errors are the standard deviation.

^aThe assumed gas kinetic temperatures are fixed at the excitation temperatures of CH₃CCH derived by Taniguchi et al. (2018b): 33 K, 29 K, and 23 K for G12.89+0.49, G16.86–2.16, and G28.28–0.36, respectively. The assumed H₂ densities are fixed at 1×10^5 cm $^{-3}$.

^bThe assumed gas kinetic temperatures are fixed at the excitation temperatures of CH₃CCH derived by Taniguchi et al. (2018b). The assumed H₂ densities are fixed at 5×10^4 cm $^{-3}$.

^cThe assumed gas kinetic temperatures are fixed at the lower limits of excitation temperatures of CH₃CCH derived by Taniguchi et al. (2018b); 24 K, 21 K, and 17 K for G12.89+0.49, G16.86–2.16, and G28.28–0.36, respectively. The assumed H₂ densities are fixed at 1×10^5 cm $^{-3}$.

^dThe excitation temperatures are fixed at the main species derived by Taniguchi et al. (2018b).

3.2.3. CH₃CN

We derived the rotational temperatures and column densities of CH₃CN in the three sources from a rotational diagram analysis, using the following formula (Goldsmith & Langer 1999);

$$\ln \frac{3k \int T_{\text{mb}} dv}{8\pi^3 \nu S \mu^2} = \ln \frac{N}{Q(T_{\text{rot}})} - \frac{E_{\text{up}}}{kT_{\text{rot}}}, \quad (4)$$

where S is the line strength, E_{up} is the upper energy level, and $Q(T_{\text{rot}})$ is the partition function for the rotational temperature T_{rot} . The electric dipole moment of CH₃CN is 3.92197 D (Pickett et al. 1998). The $\int T_{\text{mb}} dv$ integral represents the integrated intensity values summarized in Table 2.

The rotational diagrams for each source are shown in the bottom panels of Figure 3. In the case of G12.89+0.49 and G16.86–2.16, we excluded the $J_K = 5_4 - 4_4$ line ($E_{\text{up}}/k = 127.5$ K) from the fitting, because the fitting results are significantly bad if we include this point. We conjecture that contributions of inner hot regions for this line are larger than those for other lines. In fact, the line widths of the $J_K = 5_4 - 4_4$ line are significantly larger than those of other CH₃CN lines (Table 2). The derived column densities and rotational temperatures are $1.2_{-0.4}^{+1.2} \times 10^{14}$ cm $^{-2}$ and 119_{-36}^{+85} K in G12.89+0.49, $4.5_{-0.9}^{+1.8} \times 10^{13}$ cm $^{-2}$ and 68_{-15}^{+26} K in G16.86–2.16, and $5.1_{-0.8}^{+1.1} \times 10^{12}$ cm $^{-2}$ and 36_{-8}^{+11} K in G28.28–0.36, respectively (see Table 3).

We do not know sizes of the emission regions and so could not apply a beam dilution correction for each line. The analyses without the beam dilution correction may overestimate the rotational temperature and underestimate the column density.

4. DISCUSSION

4.1. Comparison of the CCH/HC₅N ratio between MYSOs and WCCC sources

As mentioned in Section 1, the CCH/HC₅N ratio can probably be used as a temperature probe for regions where carbon-chain molecules exist. In this subsection, we will compare the CCH/HC₅N ratio among MYSOs and a low-mass WCCC source.

We summarize the CCH/HC₅N ratio around both the three high-mass protostars and one low-mass protostar (L1527) in Table 4. We estimated the errors for the most severe cases to confirm that the CCH/HC₅N ratios in MYSOs are clearly different from that in L1527.

Table 4. Comparison of the CCH/HC₅N ratio around young protostars

Source Type	MYSOs			Low-mass WCCC source
Source	G12.89+0.49 ^a	G16.86–2.16 ^a	G28.28–0.36 ^a	L1527 ^b
CCH/HC ₅ N	17 ⁺⁸ ₋₇	17 ⁺⁶ ₋₅	14 ⁺⁶ ₋₇	625 ⁺³⁰⁴¹ ₋₃₃₉

NOTE—The upper and lower errors were calculated as $[N(\text{CCH}) \pm \delta N(\text{CCH})] / [N(\text{HC}_5\text{N}) \mp \delta N(\text{HC}_5\text{N})]$, where $\delta N(\text{species})$ represents the standard deviation of the column densities.

^a The column densities of HC₅N were taken from Taniguchi et al. (2017b); $2.39^{+0.15}_{-0.17} \times 10^{13} \text{ cm}^{-2}$, $2.78^{+0.16}_{-0.2} \times 10^{13} \text{ cm}^{-2}$, and $2.05^{+0.2}_{-0.05} \times 10^{13} \text{ cm}^{-2}$ in G12.89+0.49, G16.86–2.16, and G28.28–0.36, respectively.

^b The column densities of HC₅N and CCH were taken from Yoshida et al. (2019).

The column densities of HC₅N were previously derived to be $2.39^{+0.15}_{-0.17} \times 10^{13} \text{ cm}^{-2}$, $2.78^{+0.16}_{-0.2} \times 10^{13} \text{ cm}^{-2}$, and $2.05^{+0.2}_{-0.05} \times 10^{13} \text{ cm}^{-2}$ in G12.89+0.49, G16.86–2.16, and G28.28–0.36, respectively (Taniguchi et al. 2017b). These column densities were derived by the rotational diagram method using ten lines with upper state energies of 7.0 – 99.7 K. Using the column densities of CCH summarized in Table 3, the CCH/HC₅N ratios are calculated to be 17^{+8}_{-7} , 17^{+6}_{-5} , and 14^{+6}_{-7} in each MYSO. These high-mass values were obtained using the column densities of CCH in case “c” in Table 3. The errors cover all of the three cases. These CCH/HC₅N ratios are the averaged values over the Nobeyama beam size of 18”.

For L1527, the low-mass WCCC source, Yoshida et al. (2019) derived the column density and excitation temperature of HC₅N to be $(2.4 \pm 1.8) \times 10^{12} \text{ cm}^{-2}$ and $22 \pm 7 \text{ K}$, respectively. Yoshida et al. (2019) derived the CCH column density in L1527 to be $(1.2\text{--}2.2) \times 10^{15} \text{ cm}^{-2}$ and $(1.5 \pm 0.3) \times 10^{15} \text{ cm}^{-2}$ by non-LTE and LTE methods, respectively. Thus, the CCH/HC₅N ratio in L1527 is 625^{+3041}_{-339} .

We clearly recognize a difference in the CCH/HC₅N ratio between MYSOs and the L1527 low-mass WCCC source (see Table 4). Specifically, the CCH/HC₅N ratios in MYSOs are lower than that in the low-mass WCCC source by one order of magnitude at least, suggesting that the carbon-chain chemistry around MYSOs is different from that in low-mass counterparts.

4.2. Temperature dependence of the CCH/HC₅N ratio

We now compare the observed CCH/HC₅N ratios with the modeled values. Taniguchi et al. (2019a) ran time-dependent chemical simulations of hot-core models with a warm-up period using the state-of-the-art three-phase chemical code Nautilus (Ruaud et al. 2016). In this section, we first use the results with a slow warm-up period ($1 \times 10^6 \text{ yr}$) between 15 and 185 K, because our primary goal is to investigate the temperature dependence of the CCH/HC₅N ratio in detail. Later we will use a faster warm-up period for comparison.

Panel (a) of Figure 4 shows comparisons between the observed CCH/HC₅N ratios in MYSOs (orange horizontal line) and L1527 (blue horizontal line) along with the modeled value as a function of temperature. The modeled CCH/HC₅N ratio generally decreases as the temperature increases. The observed CCH/HC₅N values in the MYSOs agree best with the modeled value at $T \simeq 85 \text{ K}$. In the case of L1527, there are some regions where the observed value is reproduced by the model calculation, but the most likely point is at $T \simeq 35 \text{ K}$, taking the distributions of carbon-chain species in L1527 (Sakai et al. 2010) and the profile of the gas temperature (e.g., van ’t Hoff et al. 2018) into consideration. This temperature almost agrees with the carbon-chain spatial distribution in L1527 (Sakai et al. 2010) and matches the WCCC model (Hassel et al. 2008).

Panel (b) of Figure 4 shows the result of a fast warm-up period ($5 \times 10^4 \text{ yr}$) with the same cosmic ray ionization rate ($1.3 \times 10^{-17} \text{ s}^{-1}$) as Panel (a). The observed CCH/HC₅N ratio agrees with the model at $T \simeq 87 \text{ K}$, which is consistent with the temperature suggested from Panel (a) of $\approx 85 \text{ K}$.

To summarize, carbon-chain species around MYSOs exist in higher temperature regions than those in low-mass WCCC sources. This suggestion is also supported by the facts that the CCH column densities in the MYSOs are lower than those in the low-mass WCCC sources, while the HC₅N column densities in the MYSOs are higher than those

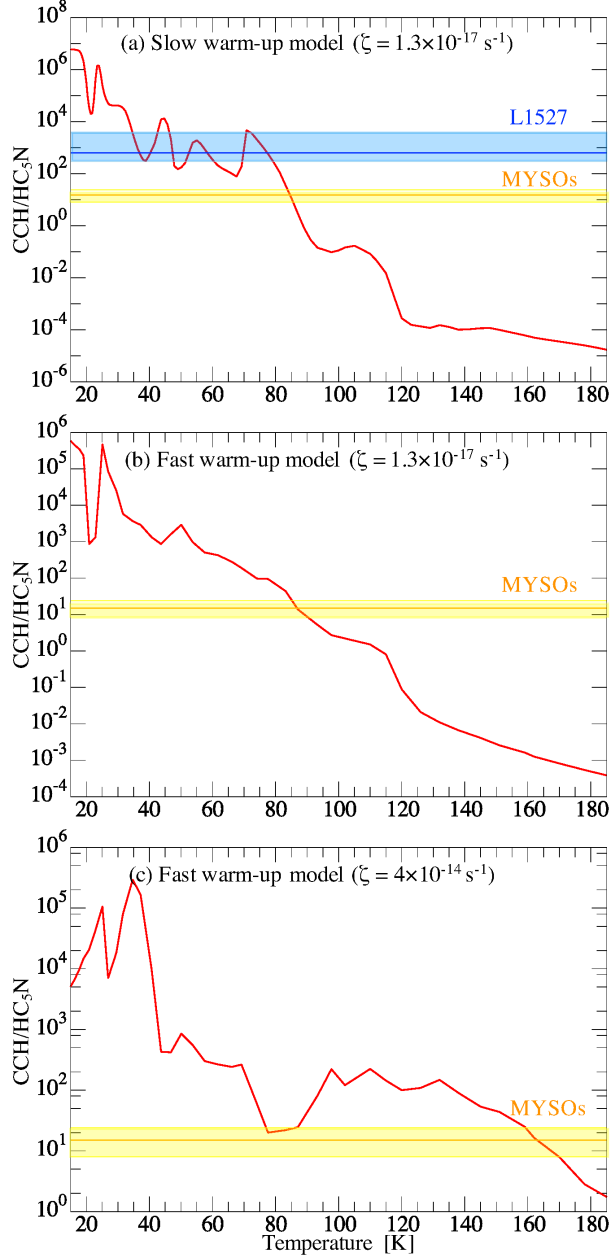


Figure 4. Comparisons of the CCH/HC₅N ratio between the observed values and the model calculations (Taniguchi et al. 2019a). The red curves show the modeled CCH/HC₅N ratio in (a) the Slow warm-up period (1×10^6 yr) model with $\zeta = 1.3 \times 10^{-17} \text{ s}^{-1}$, (b) the Fast warm-up period (5×10^4 yr) model with $\zeta = 1.3 \times 10^{-17} \text{ s}^{-1}$ and (c) the Fast warm-up period (5×10^4 yr) model with $\zeta = 4.0 \times 10^{-14} \text{ s}^{-1}$. The orange line indicates the observed value in G28.28–0.36 and the yellow range covers the observed values in the three MYSOs including the standard deviation. The blue line in panel (a) indicates the observed value in L1527 and the blue range covers the observed error in L1527.

in the low-mass counterparts by more than one order of magnitude. These results may indicate that HC₅N exists in higher temperature regions where CCH is deficient around the MYSOs, as discussed in detail later.

Distributions of carbon-chain species could be extended to cold and/or lukewarm envelopes too (e.g., Bianchi et al. 2019). In that case, the observed CCH/HC₅N ratios should be considered as the upper limits because of the mixing with low-temperature components. Such contributions from the low-temperature components are expected to be larger in MYSOs than those in low-mass protostars. This means that the temperature where carbon-chain species exist around MYSOs estimated from the above comparison is the lower limit, and our conclusion that carbon-chain

molecules around MYSOs exist in higher temperature regions compared to those around low-mass WCCC sources does not change. In fact, Taniguchi et al. (2019a) suggested that the observed lower limit of the HC₅N abundance and the observed HC₅N/CH₃OH ratio in G28.28–0.36 can be reproduced when the temperature reaches the desorption temperature of HC₅N ($T \approx 115$ K). Thus, HC₅N around MYSOs could exist in hot-core regions with temperatures above 100 K.

Comparisons of ratios between molecular column densities are more reliable than those of fractional abundances with respect to H₂, mainly because of large uncertainties in deriving H₂ column densities. Hence, we conclude that HC₅N around MYSOs exists in higher temperature regions than in the low-mass WCCC case. In such temperature regimes, CCH seems to be destroyed efficiently by reactions with O ($T \leq 90$ K) and H₂ ($T \geq 90$ K). On the other hand, the gas-phase HC₅N molecules are removed mainly by reactions with HCO⁺ and by adsorption onto dust grains. The gas-phase HCO⁺ abundance is much lower than those of O and H₂ by a few orders of magnitude. Therefore, the destruction rate of HC₅N is slower than that of CCH in such high temperature conditions. In fact, the CCH column densities in MYSOs are lower than those in low-mass WCCC sources, while the HC₅N column densities in MYSOs are higher than those in low-mass WCCC sources. This implies that CCH is possibly destroyed more efficiently in high-mass star forming regions in larger scales because of the higher temperature. A similar conclusion that CCH is efficiently destroyed around massive stars has also been reached in previous studies (e.g., Jiang et al. 2015). Moreover, the possibility of more efficient destruction of carbon-chain species by atomic oxygen in high-mass star-forming regions compared to that in low-mass counterparts was suggested by Taniguchi et al. (2018c).

Panel (c) of Figure 4 shows the model result with a high cosmic ray ionization rate of $4 \times 10^{-14} \text{ s}^{-1}$ and a fast warm-up period ($5 \times 10^4 \text{ yr}$) taken from Taniguchi et al. (2019a). We present only the fast warm-up model because the observed HC₅N abundance could not be reproduced in the slow warm-up model and the high cosmic-ray ionization rate (see Taniguchi et al. 2019a). Such a high cosmic ray ionization rate could be possible in protostellar systems (Padovani et al. 2016), and abundances of a few carbon-chain species in the OMC-2 FIR 4 young intermediate-mass protoclusters can be reproduced with this high cosmic ray ionization rate (Fontani et al. 2017; Favre et al. 2018). In this model, the observed CCH/HC₅N ratios in MYSOs can be explained at temperatures of ~ 80 K and ~ 160 K. Since the observed CCH/HC₅N ratios are possibly the upper limits as discussed before, temperatures above 160 K are not omitted, while the observed ratios cannot be reproduced by the model at temperatures of $\sim 90 - 160$ K. Again, the suggested temperatures where carbon-chain species exist ($\simeq 80$ K and ≥ 160 K) are higher than those in the low-mass WCCC source.

4.3. ¹³C Isotopic Fractionation of HC₃N in MYSOs

During the observations presented in this paper, we have detected the three ¹³C isotopologues of HC₃N in the three MYSOs. We summarize the derived ¹²C/¹³C ratios of HC₃N in the three MYSOs in Table 5. The ¹²C/¹³C ratio depends on the distance from the Galactic Center, hereafter D_{GC} (e.g., Milam et al. 2005). In Table 5, we listed the predicted ¹²C/¹³C ratios derived by the following formula (Yan et al. 2019):

$$^{12}\text{C}/^{13}\text{C} = (5.08 \pm 1.10) \times D_{\text{GC}} + (11.86 \pm 6.60). \quad (5)$$

The D_{GC} values are estimated at 5.2 kpc, 6.4 kpc, and 5.5 kpc for G12.89+0.49, G16.86–2.16, and G28.28–0.36, respectively, applying the law of cosines and assuming that the distance between the Galactic Center and the Sun is 8 kpc (Eisenhauer et al. 2003). The observed ¹²C/¹³C ratios in the three MYSOs almost agree with the predicted values within their errors. This means that the dilution of the ¹³C species does not occur for HC₃N, which was also found in nearby low-mass starless cores (Taniguchi et al. 2017a, 2019b). The ¹²C/¹³C ratios will change if the excitation temperatures of the ¹³C isotopologues are different from those of the ¹²C species. Thus, we do not discuss the matter in further detail, because we derived the column densities of the ¹³C isotopologues with fixed excitation temperatures (Section 3.2.2).

We derived the column density ratios of [H¹³CCCN] : [HC¹³CCN] : [HCC¹³CN], namely the ¹³C isotopic fractionation, and the results are summarized in Table 6. Taniguchi et al. (2016b) determined these ratios to be 1.0 (± 0.2) : 1.00 : 1.47 (± 0.17) (1σ) in G28.28–0.36 with higher velocity resolution (0.5 km s^{-1}) spectra. The ratios derived in this paper in G28.28–0.36 show a similar tendency; the abundances of H¹³CCCN and HC¹³CCN are comparable to each other, and the abundance of HCC¹³CN is higher than the others. On the other hand, in G12.89+0.49 and G16.86–2.16, we could not recognize any differences in abundance among the ¹³C isotopologues.

Table 5. $^{12}\text{C}/^{13}\text{C}$ ratio of HC_3N in the three MYSOs

	G12.89+0.49	G16.86–2.16	G28.28–0.36
H^{13}CCCN	25^{+4}_{-3}	32^{+5}_{-4}	31^{+6}_{-10}
HC^{13}CCN	23^{+3}_{-2}	31 ± 4	30^{+2}_{-9}
HCC^{13}CN	25^{+4}_{-3}	30 ± 4	24^{+1}_{-7}
Average	24	31	28
Prediction ^a	26–51	31 – 58	27 – 52

NOTE—The column densities of the main isotopologue were derived to be $4.4 \times 10^{13} \text{ cm}^{-2}$, $4.3 \times 10^{13} \text{ cm}^{-2}$, and $2.0 \times 10^{13} \text{ cm}^{-2}$ in G12.89+0.49, G16.86–2.16, and G28.28–0.36, respectively (Taniguchi et al. 2018b). The errors are the standard deviation.

^a Calculated using the formula derived by Yan et al. (2019).

Table 6. The ^{13}C isotopic fractionation of HC_3N in the three MYSOs

Source	$[\text{H}^{13}\text{CCCN}] : [\text{HC}^{13}\text{CCN}] : [\text{HCC}^{13}\text{CN}]$
G12.89+0.49	0.92 (± 0.12) : 1.00 : 0.90 (± 0.11)
G16.86–2.16	0.96 (± 0.14) : 1.00 : 1.00 (± 0.14)
G28.28–0.36	1.0 (± 0.3) : 1.0 : 1.3 (± 0.2)

NOTE—The errors are the standard deviation.

Based on the ^{13}C isotopic fractionation patterns, we can constrain the main formation pathways of carbon-chain species (e.g., Taniguchi et al. 2016a; Burkhardt et al. 2018). Regarding HC_3N , three fractionation patterns and corresponding formation pathways were proposed (Taniguchi et al. 2016b, 2017a):

1. If the abundance ratios are $[\text{H}^{13}\text{CCCN}] : [\text{HC}^{13}\text{CCN}] : [\text{HCC}^{13}\text{CN}] = 1 : 1 : x$ (x is an arbitrary value), the reaction “ $\text{C}_2\text{H}_2 + \text{CN}$ ” is dominant.
2. If the abundance ratios are $[\text{H}^{13}\text{CCCN}] : [\text{HC}^{13}\text{CCN}] : [\text{HCC}^{13}\text{CN}] = y : 1 : z$ (y and z are arbitrary values), the reaction “ $\text{CCH} + \text{HNC}$ ” is dominant.
3. If the abundance ratios are $[\text{H}^{13}\text{CCCN}] : [\text{HC}^{13}\text{CCN}] : [\text{HCC}^{13}\text{CN}] \approx 1 : 1 : 1$, the electron recombination reaction of HC_3NH^+ is dominant.

The third pathway is a hypothesis, because Taniguchi et al. (2017a) assumed that there are competitive formation pathways of HC_3NH^+ , which have not been confirmed by any observations. According to the above classification, the main formation pathway of HC_3N is the electron recombination reaction of HC_3NH^+ in G12.89+0.49 and G16.86–2.16. In G28.28–0.36, the reaction between C_2H_2 and CN is dominant, which agrees with the conclusion by Taniguchi et al. (2016b). We will discuss a possible explanation for the difference in the main formation mechanism of HC_3N between G28.28–0.36 and the others in the next subsection.

4.4. Constraints of ages of MYSOs based on the $\text{CCH}/\text{HC}_5\text{N}$ ratio and the ^{13}C isotopic fractionation of HC_3N

We constrain the age and possible carbon-chain chemistry in each MYSO based on the $\text{CCH}/\text{HC}_5\text{N}$ ratio (Section 4.2) and the ^{13}C isotopic fractionation of HC_3N (Section 4.3). Figure 5 shows the time dependence of the $\text{CCH}/\text{HC}_5\text{N}$ ratio and temperature during the warm-up period (Taniguchi et al. 2019a). The data are the same as in Figure 4. Figure 6 shows the time dependence of contributions for each formation pathway of HC_3N . The basic formation and destruction mechanisms of carbon-chain species do not change between the different warm-up periods with the same cosmic ray ionization rate ($1.3 \times 10^{-17} \text{ s}^{-1}$) (Taniguchi et al. 2019a). Since the formation and destruction mechanisms

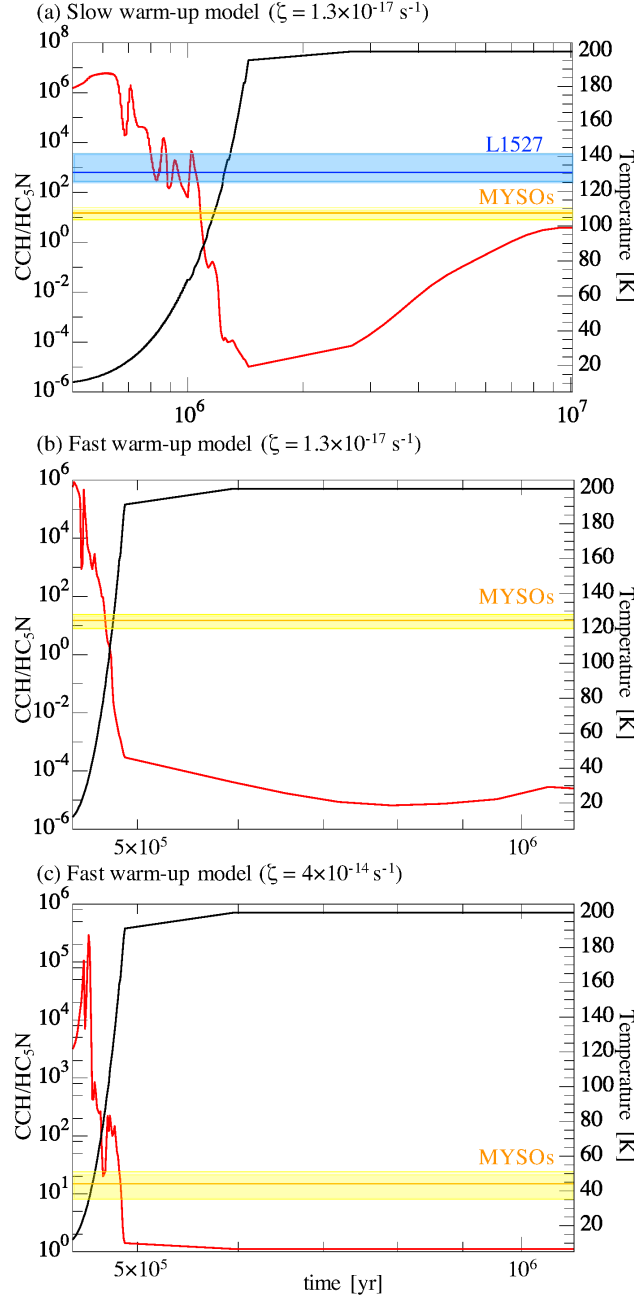


Figure 5. Comparisons of the CCH/HC₅N ratio between the observed values and the model calculations (Taniguchi et al. 2019a). The red and black curves show the modeled CCH/HC₅N ratio and temperature, respectively, in (a) the Slow warm-up period model with $\zeta = 1.3 \times 10^{-17} \text{ s}^{-1}$, (b) the Fast warm-up period ($5 \times 10^4 \text{ yr}$) model with $\zeta = 1.3 \times 10^{-17} \text{ s}^{-1}$, and (c) the Fast warm-up period model with $\zeta = 4.0 \times 10^{-14} \text{ s}^{-1}$. The orange line indicates the observed value in G28.28–0.36 and the yellow range covers the observed values in the three MYSOs including the standard deviation. The blue line in panel (a) indicates the observed value in L1527 and the blue range covers the error in L1527.

depend on the temperature, the age value will change but our discussions need not change. We can investigate the time-dependence of the formation pathways of HC₃N in detail using the model with the slow warm-up period, and so presented this model here. The results of the fast warm-up period with a cosmic ray ionization rate of $1.3 \times 10^{-17} \text{ s}^{-1}$ were not presented in Figure 6, because we were not able to find any new results.

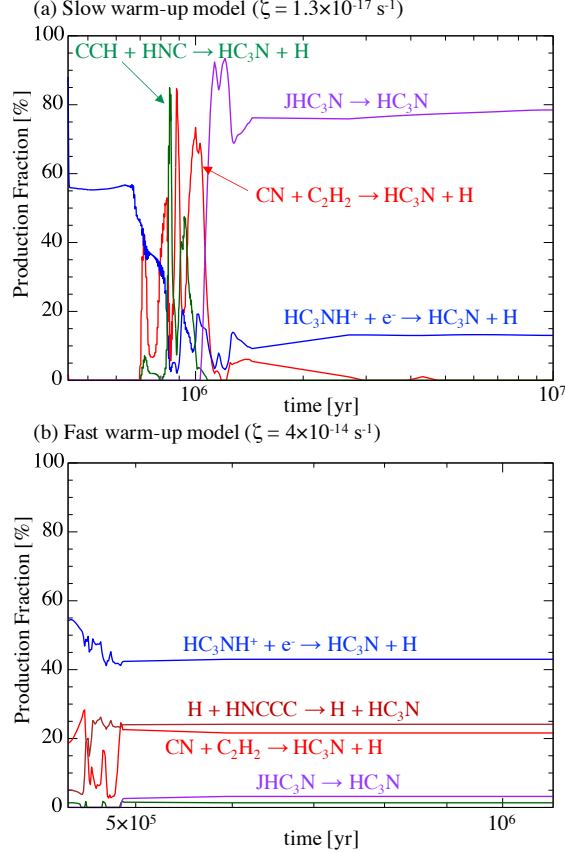


Figure 6. Production fraction of formation pathways of HC_3N during the warm-up period (Taniguchi et al. 2019a). JHC_3N denotes molecules on the dust surface.

As discussed in Section 4.2, the observed $\text{CCH}/\text{HC}_5\text{N}$ ratios in MYSOs agree with the model at a temperature of $\sim 85 \text{ K}$. This temperature corresponds to $1.08 \times 10^6 \text{ yr}^5$, as shown in panel (a) of Figure 5. Just before this time ($t < 1.07 \times 10^6 \text{ yr}$), the main formation pathway of HC_3N is the reaction between C_2H_2 and CN (panel (a) of Figure 6). This is consistent with the reaction proposed based on the ^{13}C isotopic fractionation in G28.28–0.36.

The electron recombination reaction of HC_3NH^+ is dominant in the model with the high cosmic ray ionization rate during the whole warm-up period (panel (b) of Figure 6). Thus, the ^{13}C isotopic fractionation of HC_3N in G12.89+0.49 and G16.86–2.16 can be explained by this high cosmic ray ionization rate model. These results suggest that the cosmic ray ionization rates in G12.89+0.49 and G16.86–2.16 may be higher than that in G28.28–0.36 or physical structures in G12.89+0.49 and G16.86–2.16 allow cosmic rays to penetrate into regions where carbon-chain species are formed. The observed $\text{CCH}/\text{HC}_5\text{N}$ ratios in MYSOs agree with the age of $(4.7\text{--}4.86) \times 10^5 \text{ yr}$ as indicated in panel (c) of Figure 5.

In summary, the observed $\text{CCH}/\text{HC}_5\text{N}$ ratios around MYSOs can be reproduced in the chemical network simulations at a given temperature and time. Taking the ^{13}C isotopic fractionation of HC_3N into consideration, G12.89+0.49 and G16.86–2.16 may prefer the model with the high cosmic ray ionization rate ($\zeta = 4 \times 10^{-14} \text{ s}^{-1}$), while G28.28–0.36 agrees with the model with the standard cosmic ray ionization rate ($\zeta = 1.3 \times 10^{-17} \text{ s}^{-1}$). These results imply that carbon-chain chemistry in G12.89+0.49 and G16.86–2.16 may resemble that in the OMC-2 FIR 4 young intermediate-mass protoclusters (Fontani et al. 2017; Favre et al. 2018), but that in G28.28–0.36 is different from the other MYSOs and OMC-2 FIR 4. The clear ^{13}C isotopic fractionation of HC_3N in G28.28–0.36 supports its bottom-up formation during the warm-up stage, while carbon-chain species, at least HC_5N , exist in higher temperature regions than those in low-mass WCCC sources. Different chemical pathways are present because of the possibly different physical conditions,

⁵ This age does not mean a physical age of a MYSO, because we derive the age from the chemical network simulations and the age will change by the assumed warm-up timescales.

as suggested by our chemical code. Future observations with interferometers such as ALMA will clarify such a new type of carbon-chain chemistry around MYSOs.

5. CONCLUSIONS

We have carried out observations of the rotational lines of CCH ($N = 1 - 0$), CH_3CN ($J = 5 - 4$), and three ^{13}C isotopologues of HC_3N ($J = 10 - 9$) toward the three MYSOs, G12.89+0.49, G16.86-2.16, and G28.28-0.36, with the Nobeyama 45-m telescope. The observational results and main conclusions are as follows:

1. We determined the CCH/ HC_5N ratios, which are considered as a temperature probe where carbon-chain species exist in the three MYSOs. The CCH/ HC_5N ratios are derived to be ~ 15 in the MYSOs. These CCH/ HC_5N ratios in the MYSOs are lower than those in low-mass WCCC sources by more than one order of magnitude.
2. We compare these observational values to the chemical network simulations with a warm-up period. The observed CCH/ HC_5N ratios in the MYSOs are reproduced when the temperature reaches ~ 85 K, while that in L1527 agrees with the model at a temperature of ~ 35 K. In the model calculation with the high cosmic ray ionization rate ($4 \times 10^{-14} \text{ s}^{-1}$), the observed CCH/ HC_5N ratios in the MYSOs can be reproduced at temperatures of ~ 80 K and ~ 160 K. Hence, HC_5N detected around the MYSOs exists preferentially in higher temperature regions than that in low-mass WCCC sources. In such temperature regimes ($T \geq 70$ K), CCH, which is a reactive species, is efficiently destroyed by reactions with O and/or H_2 .
3. We determined the ^{13}C isotopic fractionation of HC_3N in the three MYSOs. All of the three ^{13}C isotopologues of HC_3N show similar column densities in G12.89+0.49 and G16.86-2.16, while HCC^{13}CN is more abundant than the others in G28.28-0.36. Based on the results, the electron recombination reaction of HC_3NH^+ is proposed as the main formation pathway of HC_3N in G12.89+0.49 and G16.86-2.16. This is consistent with the model with the high cosmic ray ionization rate. On the other hand, in G28.28-0.36, the main formation pathway of HC_3N is the reaction between C_2H_2 and CN. This reaction is dominant in the model with the standard cosmic ray ionization rate ($1.3 \times 10^{-17} \text{ s}^{-1}$).

Based on the CCH/ HC_5N ratio and the ^{13}C isotopic fractionation, the carbon-chain chemistry in the G28.28-0.36 MYSO seems to be different from that in the other two MYSOs, OMC-2 FIR 4 (Fontani et al. 2017; Favre et al. 2018), and low-mass WCCC sources. In this source, cyanopolynes are likely formed by the bottom-up mechanism during the lukewarm regions ($25 < T < 50$ K) and exist in higher temperature regions ($T \gtrsim 85$ K) than in low-mass WCCC sources.

ACKNOWLEDGMENTS

We would like to express our special thanks to the staff of the Nobeyama Radio Observatory. The Nobeyama Radio Observatory is a branch of the National Astronomical Observatory of Japan, National Institutes of Natural Sciences. K.T. would like to thank the University of Virginia for providing the funds for her postdoctoral fellowship in the Virginia Initiative on Cosmic Origins (VICO) research program. This work was supported by JSPS KAKENHI Grant Number JP20K14523. E.H. thanks the National Science Foundation for support through grant AST-1906489. ZYL is supported in part by NSF AST-1910106 and NASA 80NSSC20K0533. JCT acknowledges ERC grant MSTAR and VR grant 2017-04522.

Facilities: Nobeyama 45-m radio telescope

Software: NEWSTAR, Nautilus (Ruard et al. 2016)

REFERENCES

- Balucani, N., Ceccarelli, C., & Taquet, V. 2015, MNRAS, 449, L16
- Benson, P. J., Caselli, P., & Myers, P. C. 1998, ApJ, 506, 743

- Bianchi, E., Ceccarelli, C., Codella, C., et al. 2019, *ACS Earth and Space Chemistry*, 3, 2659
- Burkhardt, A. M., Herbst, E., Kalenskii, S. V., et al. 2018, *MNRAS*, 474, 5068
- Crockett, N. R., Bergin, E. A., Neill, J. L., et al. 2015, *ApJ*, 806, 239
- Cyganowski, C. J., Brogan, C. L., Hunter, T. R., et al. 2011, *ApJ*, 743, 56
- Cyganowski, C. J., Whitney, B. A., Holden, E., et al. 2008, *AJ*, 136, 2391
- DeLeon, R. L., & Muentzer, J. S. 1985, *JChPh*, 82, 1702
- Eisenhauer, F., Schödel, R., Genzel, R., et al. 2003, *ApJL*, 597, L121
- Favre, C., Ceccarelli, C., López-Sepulcre, A., et al. 2018, *ApJ*, 859, 136
- Fontani, F., Ceccarelli, C., Favre, C., et al. 2017, *A&A*, 605, A57
- Garrod, R. T., & Herbst, E. 2006, *A&A*, 457, 927
- Garrod, R. T., Widicus Weaver, S. L., & Herbst, E. 2008, *ApJ*, 682, 283
- Goldsmith, P. F., & Langer, W. D. 1999, *ApJ*, 517, 209
- Green, C.-E., Green, J. A., Burton, M. G., et al. 2014, *MNRAS*, 443, 2252
- Hassel, G. E., Herbst, E., & Garrod, R. T. 2008, *ApJ*, 681, 1385
- Herbst, E., & van Dishoeck, E. F. 2009, *ARA&A*, 47, 427
- Immer, K., Reid, M. J., Menten, K. M., et al. 2013, *A&A*, 553, A117
- Jiang, X.-J., Liu, H. B., Zhang, Q., et al. 2015, *ApJ*, 808, 114
- Jorgensen, J. K., Belloche, A., & Garrod, R. T. 2020, arXiv e-prints, arXiv:2006.07071
- Li, F. C., Xu, Y., Wu, Y. W., et al. 2016, *AJ*, 152, 92
- Lu, X., Zhang, Q., Liu, H. B., et al. 2014, *ApJ*, 790, 84
- McGuire, B. A. 2018, *ApJS*, 239, 17
- Milam, S. N., Savage, C., Brewster, M. A., et al. 2005, *ApJ*, 634, 1126
- Minamidani, T., Nishimura, A., Miyamoto, Y., et al. 2016, *Proc. SPIE*, 99141Z
- Müller, H. S. P., Schlöder, F., Stutzki, J., et al. 2005, *Journal of Molecular Structure*, 742, 215
- Nomura, H., & Millar, T. J. 2004, *A&A*, 414, 409
- Padovani, M., Marcowith, A., Hennebelle, P., et al. 2016, *A&A*, 590, A8
- Panagia, N. 1973, *AJ*, 78, 929
- Pickett, H. M., Poynter, R. L., Cohen, E. A., et al. 1998, *JQSRT*, 60, 883
- Purcell, C. R., Balasubramanyam, R., Burton, M. G., et al. 2006, *MNRAS*, 367, 553
- Ruaud, M., Wakelam, V., & Hersant, F. 2016, *MNRAS*, 459, 3756
- Sakai, N., Sakai, T., Hirota, T., et al. 2010, *ApJ*, 722, 1633
- Sakai, N., & Yamamoto, S. 2013, *Chemical Reviews*, 113, 8981
- Skouteris, D., Balucani, N., Ceccarelli, C., et al. 2019, *MNRAS*, 482, 3567
- Suzuki, H., Yamamoto, S., Ohishi, M., et al. 1992, *ApJ*, 392, 551
- Taniguchi, K., Herbst, E., Caselli, P., et al. 2019a, *ApJ*, 881, 57
- Taniguchi, K., Herbst, E., Ozeki, H., et al. 2019b, *ApJ*, 884, 167
- Taniguchi, K., Miyamoto, Y., Saito, M., et al. 2018a, *ApJ*, 866, 32
- Taniguchi, K., Ozeki, H., Saito, M., et al. 2016a, *ApJ*, 817, 147
- Taniguchi, K., Ozeki, H., & Saito, M. 2017a, *ApJ*, 846, 46
- Taniguchi, K., Saito, M., Hirota, T., et al. 2017b, *ApJ*, 844, 68
- Taniguchi, K., Saito, M., Majumdar, L., et al. 2018b, *ApJ*, 866, 150
- Taniguchi, K., Saito, M., & Ozeki, H. 2016b, *ApJ*, 830, 106
- Taniguchi, K., Saito, M., Sridharan, T. K., et al. 2018c, *ApJ*, 854, 133
- Tercero, B., Cuadrado, S., López, A., et al. 2018, *A&A*, 620, L6
- Urquhart, J. S., Moore, T. J. T., Menten, K. M., et al. 2015, *MNRAS*, 446, 3461
- van der Tak, F. F. S., Black, J. H., Schöier, F. L., et al. 2007, *A&A*, 468, 627
- van 't Hoff, M. L. R., Tobin, J. J., Harsono, D., et al. 2018, *A&A*, 615, A83
- Yan, Y. T., Zhang, J. S., Henkel, C., et al. 2019, *ApJ*, 877, 154
- Yoshida, K., Sakai, N., Nishimura, Y., et al. 2019, *PASJ*, 71, S18